

Breaking linear scaling relationships in oxygen evolution via dynamic structural regulation of active sites

Received: 26 May 2024

Accepted: 3 December 2024

Published online: 03 February 2025



Zheye Zhang^{1,11}, Hongyan Zhao^{2,11}, Shibo Xi^{3,11}, Xiaoxu Zhao⁴, Xiao Chi⁵, Hong Bin Yang⁶, Zhongxin Chen⁷, Xiaojiang Yu⁸, Yang-Gang Wang²✉, Bin Liu^{9,10}✉ & Peng Chen¹✉

The universal linear scaling relationships between the adsorption energies of reactive intermediates limit the performance of catalysts in multi-step catalytic reactions. Here, we show how these scaling relationships can be circumvented in electrochemical oxygen evolution reaction by dynamic structural regulation of active sites. We construct a model Ni-Fe₂ molecular catalyst via in situ electrochemical activation, which is able to deliver a notable intrinsic oxygen evolution reaction activity. Theoretical calculations and electrokinetic studies reveal that the dynamic evolution of Ni-adsorbate coordination driven by intramolecular proton transfer can effectively alter the electronic structure of the adjacent Fe active centre during the catalytic cycle. This dynamic dual-site cooperation simultaneously lowers the free energy change associated with O–H bond cleavage and O–O bond formation, thereby disrupting the inherent scaling relationship in oxygen evolution reaction. The present study not only advances the development of molecular water oxidation catalysts, but also provides an unconventional paradigm for breaking the linear scaling relationships in multi-intermediates involved catalysis.

For multi-step catalytic reactions, it has been shown that the adsorption energies of different intermediates are correlated on conventional single-site catalysts by linear scaling relationships (LSRs)^{1,2}. While LSRs simplify the prediction of catalyst performance and help elucidate catalytic activity trends, they inevitably place intrinsic limitations on optimally adjusting adsorption of every intermediate on the catalytic site simultaneously to achieve the maximum activity and/or selectivity^{2–4}. A case in point of this

correlation-imposed reaction is the electrochemical oxygen evolution reaction (OER), which serves as an ideal anodic reaction by providing electrons and protons for hydrogen generation, CO₂ reduction, etc.^{5–7} The adsorption energies of the chemically similar oxygenated intermediates over a single active site, such as *OH, *O, and *OOH involved in OER with the widely accepted adsorbate evolution mechanism (AEM), are linearly correlated and cannot be adjusted independently^{8–10}. Such correlation-imposed constraint

¹School of Chemistry, Chemical Engineering and Biotechnology, Nanyang Technological University, Singapore, Singapore. ²Department of Chemistry and Guangdong Provincial Key Laboratory of Catalytic Chemistry, Southern University of Science and Technology, Shenzhen, China. ³Institute of Sustainability for Chemicals, Energy and Environment (ISCE2), Agency for Science, Technology and Research (A*STAR), Singapore, Singapore. ⁴School of Materials Science and Engineering, Peking University, Beijing, China. ⁵Department of Physics, National University of Singapore, Singapore, Singapore. ⁶School of Materials Science and Engineering, Suzhou University of Science and Technology, Suzhou, China. ⁷School of Science and Engineering, The Chinese University of Hong Kong, Shenzhen, China. ⁸Singapore Synchrotron Light Source, National University of Singapore, Singapore, Singapore. ⁹Department of Materials Science and Engineering, City University of Hong Kong, Hong Kong SAR, China. ¹⁰Department of Chemistry, Hong Kong Institute of Clean Energy (HKICE) & Center of Super-Diamond and Advanced Films (COSDAF), City University of Hong Kong, Hong Kong SAR, China. ¹¹These authors contributed equally: Zheye Zhang, Hongyan Zhao, Shibo Xi. ✉e-mail: wangyg@sustech.edu.cn; blui48@cityu.edu.hk; ChenPeng@ntu.edu.sg

makes it rather challenging for the maximal accomplishable catalytic performance.

On account of the ubiquitous adsorption-energy scaling relationship between $^*\text{OOH}$ and $^*\text{OH}$ on various OER electrocatalysts^{11–16}, one of the most effective strategies to break such LSR is to selectively stabilize $^*\text{OOH}$ over $^*\text{OH}$ by confining intermediates within nanoscopic channels¹⁷, introducing proton acceptors^{18–20}, and/or creating multifunctional surfaces and interfacial sites^{9,21–23}. These strategies share a common idea of engineering heterogeneity of electrocatalysts. Nevertheless, atomistic insights into complex multiphase materials or interfaces during OER are very limited and remain elusive. Specifically, few experimental attempts have been made using heterostructured catalysts, but their heterogeneous nature poses great challenges in refining the structures of the most active surficial catalytic sites for use as the synthetic targets^{20–22}. Furthermore, static structures identified through ex situ characterization cannot accurately reflect the real active sites responsible for catalytic activity under reaction conditions²⁴. These limitations greatly impede the understanding of structure–performance relationships and the rational design of next-generation high-performance OER electrocatalysts.

While structure changes in catalysts under electrochemical conditions have been extensively observed^{24–27}, the underlying coordination evolution of active sites within a catalytic cycle²⁸ and the associated intrinsic electronic origin are often overlooked. Recent studies have shown that dynamic evolution of metal-support coordination during catalysis can effectively alter the local electronic structure of the active centre^{29,30}. This dynamic regulation of the active centre enables simultaneous facilitation of reactant activation and product desorption, thereby circumventing the scaling relations in heterogeneous catalysis^{30,31}. Therefore, exploring and comprehending the local coordination evolution of active sites at the atomic scale within the OER catalytic cycle could offer the opportunity to circumvent the existing scaling relationships. Given that bimetallic Ni-Fe composites have been identified as one of the most promising OER catalysts in alkaline conditions (see Supplementary Note 1)^{15,16,32}, they can serve as an ideal platform to investigate the above hypothesis.

In this work, we report the construction of a Ni-Fe₂ molecular complex catalyst, which exhibits a notable OER performance. The catalyst preparation is based on in situ electrochemical activation of a low-coordinate Ni single-atom pre-catalyst in purified KOH electrolyte with a deliberate addition of Fe ions at ppm level. *Operando* X-ray absorption fine structure (XAFS) measurements verify the structural transformation from Ni monomer to O-bridged Ni-Fe₂ trimer during the activation process. Remarkably, by employing density functional theory (DFT) combined ab initio molecular dynamics (AIMD) simulations and electrokinetic characterization, we report an unconventional dynamic dual-site-cooperated OER mechanism, in which the Ni centre directly participates in the catalytic process to induce intramolecular proton transfer and trigger its coordination evolution. The existence of dynamic coordination between the Ni site and adsorbates (OH and H₂O) plays a key role in modulating the electronic structure of the adjacent Fe active site during the OER cycle. Such dynamic regulation contributes to lowering the free energy required for the mutually competing steps of O–H bond cleavage and $^*\text{OOH}$ formation simultaneously, which effectively surmounts the LSRs in OER. Our insights into dynamic structural evolution of active site within the catalytic cycle enlighten a path towards the development of highly efficient OER catalysts beyond the limitations of LSRs.

Results

Synthesis and characterization of the catalyst

To construct a Ni-Fe molecular complex catalyst, we first prepared a single-atom Ni pre-catalyst. As illustrated in Supplementary Fig. 1, an aqueous suspension of graphene oxide (GO) was initially sealed in a Ni

vessel at 80 °C, leading to the spontaneous assembly of a 3D Ni(OH)₂/graphene hydrogel (Supplementary Figs. 2–4)³³. After freeze-drying, the resultant aerogel was thermally annealed at 700 °C under Ar atmosphere. During which, Ni(OH)₂ was reduced to Ni/NiO nanoparticles, and simultaneously graphene nanosheet was etched into holey graphene nanomesh (GNM; Supplementary Fig. 5). Finally, acid treatment was applied to obtain Ni single atoms trapped in GNM (Ni-SAs@GNM).

Scanning electron microscopy (SEM) and transmission electron microscopy (TEM) images reveal 2D mesh structure of Ni-SAs@GNM with pore sizes in the range of ca. 20–60 nm and high nanohole density of $\sim 6.2 \times 10^9$ per cm² (Fig. 1a and Supplementary Fig. 6). The presence of crystalline Ni species in Ni-SAs@GNM is denied by high-resolution TEM (HRTEM) and X-ray diffraction (XRD) analyses (Supplementary Fig. 7). Energy-dispersive X-ray spectroscopy (EDS) elemental mappings indicate homogeneous distribution of C, O, and Ni elements (Fig. 1b). Individual dispersion of Ni atoms is confirmed by aberration-corrected high-angle annular dark-field scanning TEM (HAADF-STEM). As depicted in Fig. 1c, the bright spots corresponding to heavier Ni-SAs are evenly distributed on GNM, and it appears that Ni-SAs are predominately anchored on the edges of defects and graphitic domains (Supplementary Fig. 8). N₂ adsorption–desorption isotherm suggests mesoporous structure of Ni-SAs@GNM with a specific surface area of 266.9 m² g^{−1} (Supplementary Fig. 9). As determined by inductively coupled plasma optical emission spectroscopy (ICP-OES), the total Ni content in Ni-SAs@GNM is 0.82 wt% (Supplementary Table 1). The oxidation state of central Ni atoms is deduced to be +1 with a 3d⁹, S = 1/2 electronic configuration, as revealed by X-ray photoelectron spectroscopy (XPS) and L_{2,3}-edge X-ray absorption spectroscopy (XAS) analyses (Supplementary Fig. 10)³⁴.

Subsequently, we prepared the Ni-Fe molecular complex catalyst via an in situ electrochemical conversion process (Supplementary Fig. 11). It is worth noting that similar in situ electrochemical methods for synthesizing dual-atom catalysts have been previously reported by Hu and co-workers^{15,35}. Specially, we employed a standard three-electrode system, where Ni-SAs@GNM pre-catalyst was loaded onto a glassy carbon electrode as the working electrode. The electrochemical activation was performed using cyclic voltammetry (CV) between 1.1 and 1.65 V versus the reversible hydrogen electrode (RHE) in purified Fe-free 1 M KOH electrolyte with a deliberate addition of 1 ppm Fe ions (Fig. 1d). Alternatively, anodic chronopotentiometry and chronoamperometry can also be employed for activation (Supplementary Fig. 12). This activated catalyst is termed as Fe_{1ppm}-Ni-SAs@GNM. For comparison, Ni-SAs@GNM was also activated in Fe-free KOH electrolyte and denoted as Fe_{free}-Ni-SAs@GNM. As seen from CV curves of Fe_{1ppm}-Ni-SAs@GNM (Supplementary Fig. 13), the quasi-reversible Ni²⁺/Ni³⁺ redox peaks observed from Fe_{free}-Ni-SAs@GNM positively shift and the oxidation peak is masked by OER current, implying the formation of Ni-Fe molecular complex. Similar phenomena are observed when doping Fe into Ni hydroxides^{32,36}. Ultraviolet–visible (UV) absorption spectrum of 1 M KOH solution containing 1 ppm Fe ions shows a weak peak at 361 nm, implying the existence of Fe(OH)₄[−] (Supplementary Fig. 14)^{35,37}. It is conceivable that the negatively charged Fe(OH)₄[−] anions can be electrically driven towards the anode, which preferentially anchor on the positively charged Ni sites. The incorporation of Fe species into Ni-SAs@GNM was directly evidenced by synchrotron-based X-ray fluorescence (SXRF) spectroscopy (Fig. 1e). The atomic ratio of Ni/Fe calculated from their K α peak area is $\sim 5.2:1$, similar to that obtained from ICP-OES measurements (Supplementary Table 1). EDS elemental mappings show that both Ni and Fe are uniformly distributed (Supplementary Fig. 15a). Aberration-corrected HAADF-STEM reveals the atomic dispersion of metal elements (Supplementary Fig. 15b), while the existence of nanoparticles is ruled out by HRTEM, XRD, and Raman spectroscopy (Supplementary Fig. 15c–f).

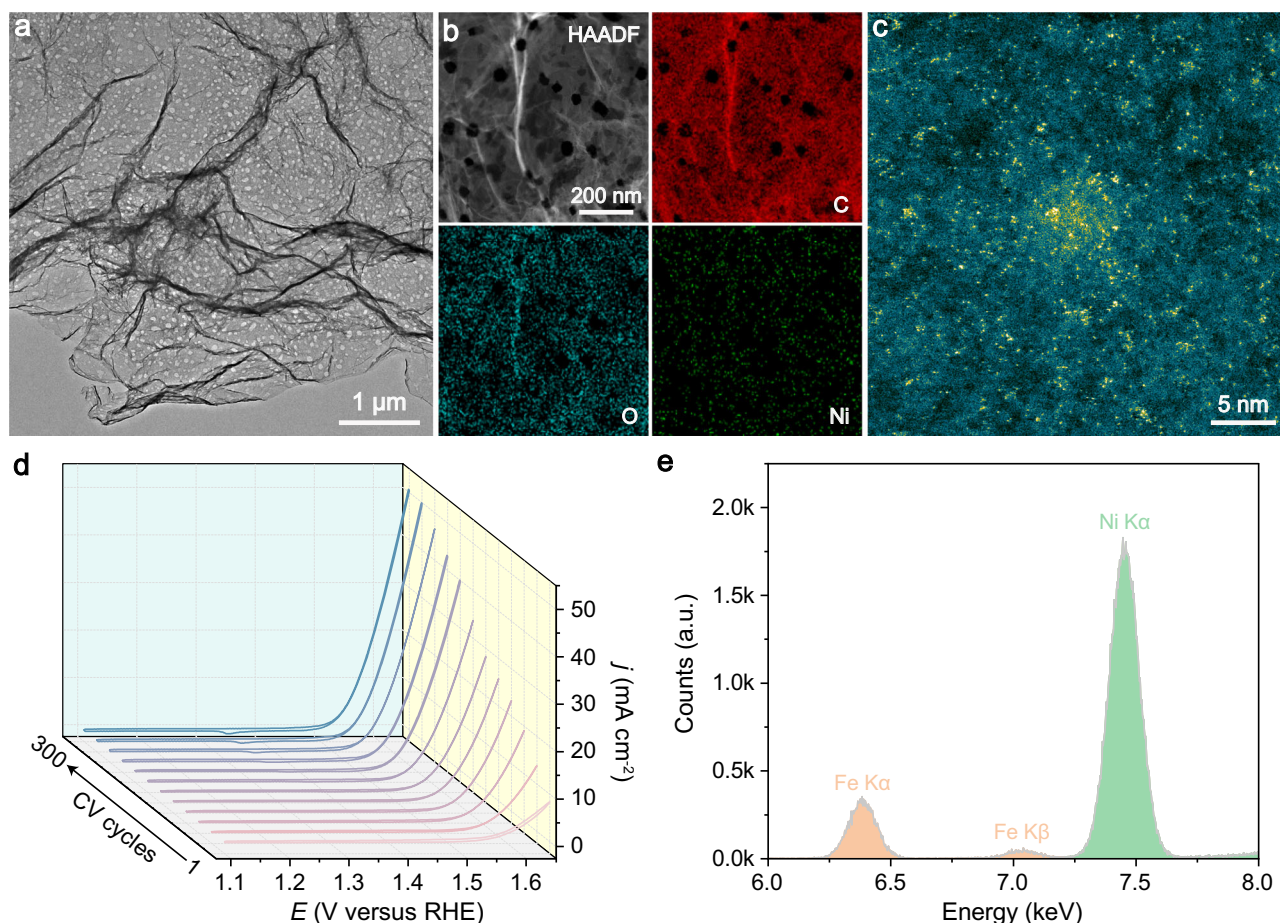


Fig. 1 | Structural characterization and electrochemical conversion process of Ni-SAs@GNM. **a–c** TEM image (**a**), the corresponding EDS element mappings (**b**), and aberration-corrected HAADF-STEM image (**c**) of Ni-SAs@GNM. **d** Repeated CV

cycles of Ni-SAs@GNM in Fe-free 1 M KOH electrolyte with a deliberate addition of 1 ppm Fe ions. **e** SXRF spectrum of the activated catalyst.

Operando XAFS analysis of Ni-Fe molecular complex catalyst

To probe the local structures of Ni/Fe atoms and the Fe incorporation dynamics during activation, *operando* XAFS^{38,39} measurements were performed (Fig. 2a and Supplementary Fig. 16). As shown in the Ni K-edge X-ray absorption near edge structure (XANES) spectra (Fig. 2b), the oxidation state of Ni in dry Ni-SAs@GNM is between 0 and +2, agreeing well with the XPS and L_{2,3}-edge XAS results (Supplementary Fig. 10). After the dry Ni-SAs@GNM sample being immersed in purified 1 M KOH, the rising edge is blue-shifted by ~2.0 eV, indicating an increase of Ni oxidation state (Fig. 2b inset), presumably due to adsorption of OH[−]. After adding 1 ppm Fe ions into purified KOH, further blue-shift in the rising edge occurs during the activation process and the energy of rising edge eventually coincided with that of the NiOOH reference (after 4 h), suggesting the formation of Ni³⁺ species. The pre-edge peak (A) at ~8332 eV can be assigned to the dipole-forbidden but quadrupole-allowed transition (1s → 3d), which signals 3d and 4p orbital hybridization of Ni centre featured broken centrosymmetry⁴⁰. This peak gradually decreases as activation continues, indicating that the coordination geometry around Ni after activation is highly centrosymmetric. The amplitude of 1s → 4p_z transition (peak B, a fingerprint for square-planar configuration⁴¹) also gradually reduces during activation, implying that the coordination configuration of Ni evolves from square-planar to octahedral. In addition, the peak at ~8350 eV (C) is attributable to the 1s → 4p_{x,y} transitions⁴². This peak gradually increases and sharpens, suggesting that the unoccupied 4p orbital becomes more localized and the energy level further degenerates,

thereby forming a highly symmetrical octahedral configuration after activation.

The structural evolution of Ni centre was further revealed by *operando* extended X-ray absorption fine structure (EXAFS) spectroscopy (Fig. 2c). The first coordination shell ranging from 1.1 to 1.5 Å is attributed to the single-scattering paths of Ni–O bond. EXAFS fitting indicates that Ni in dry Ni-SAs@GNM is most probably coordinated by two O atoms on the same plane of the graphene support (Supplementary Fig. 17 and Supplementary Table 2). The peak in the first shell gradually increases during activation, indicating that the number of coordinating O increases⁴³. Interestingly, a new peak at 2.42 ± 0.06 Å gradually appears in the second coordination shells (2.2–2.6 Å) during activation and reaches equilibrium in 4 h, implying that Fe ions continuously attach to Ni atoms via oxygen bridges^{15,35,44}. The formation of metallic Ni and Ni(OH)₂ is not evidenced. Furthermore, the coordination structure of the Ni centre after activation is similar to that in NiOOH, consistent with the XANES observation. EXAFS fitting reveals that one Ni atom is likely connected with two Fe atoms after activation, forming a Ni-Fe₂ triple-atom catalyst (Supplementary Fig. 18a, b and Supplementary Table 2).

As determined by *operando* Fe K-edge XANES spectroscopy, the amount of Fe in catalyst increases during activation, and the Fe to Ni atomic ratio eventually saturates at 1:5 (Fig. 2d, e), coinciding well with SXRF result (Fig. 1e). It is evident that the Ni content remains almost constant during activation (Supplementary Fig. 19). The lower content of Fe compared to Ni is reasonable because a considerable portion of Ni atoms may not be exposed due to the strong π–π interaction

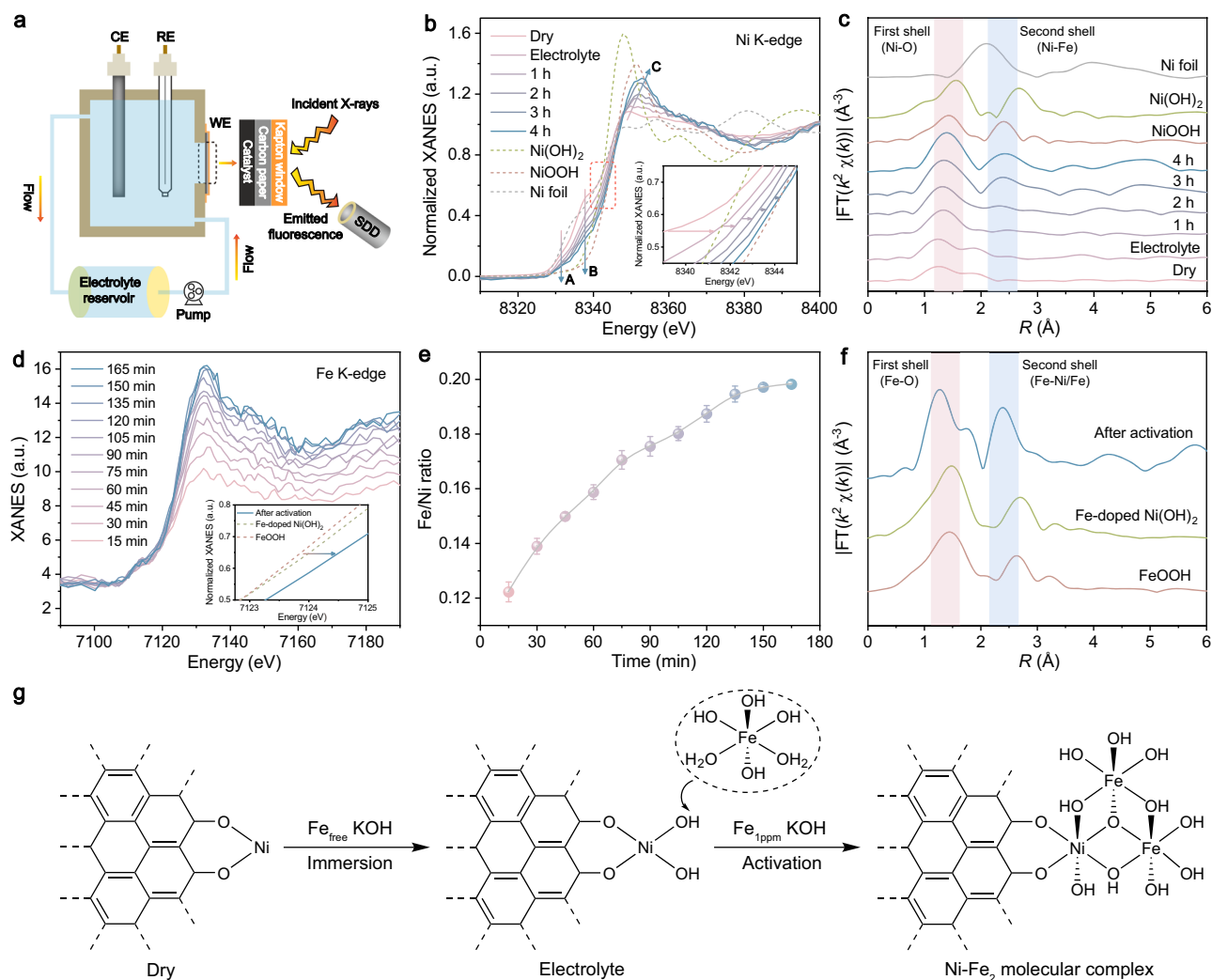


Fig. 2 | Operando XAFS measurements under OER conditions. **a** Schematic illustration of the *operando* flow cell experimental set-up. CE, counter electrode; RE, reference electrode; WE, working electrode; SDD, silicon drift detector. **b** Normalized Ni K-edge XANES spectra recorded at different activation times, with Ni foil, β -phase $\text{Ni}(\text{OH})_2$ and γ -phase NiOOH as references. Peaks A, B, and C represent $1s \rightarrow 3d$, $1s \rightarrow 4p_z$, and $1s \rightarrow 4p_{x,y}$ transitions, respectively. Inset shows a magnification of the spectra in the highlighted dashed rectangle. **c** k^2 -weighted Fourier transformation of Ni K-edge EXAFS spectra. **d** *Operando* Fe K-edge XANES

spectra recorded at different activation times. Inset shows a magnification of the normalized spectra. Fe-doped $\text{Ni}(\text{OH})_2$ and α -phase FeOOH were employed as references. **e** The plot of Fe/Ni ratio versus the activation time. The error bars are means \pm standard deviation (3 replicates). **f** k^2 -weighted Fourier transformation of Fe K-edge EXAFS spectra. In (c) and (f), the red shaded region represents the first shell, while the blue shaded region represents the second shell. **g** Proposed models for the formation of Ni-Fe_2 molecular complex catalyst.

between graphene nanosheets. Notably, the rising edge of Fe after activation is located between that of Fe^{3+} and Fe^{6+} (Fig. 2d inset and Supplementary Fig. 20), suggesting formation of Fe^{4+} species during OER^{15,36}. Fourier-transformed EXAFS spectrum for the Fe centre after activation is distinct from those of Fe-doped $\text{Ni}(\text{OH})_2$ and FeOOH , but similar to that of Ni centre after activation in the second shell (Fig. 2f), indicating that the local coordination structure of Ni and Fe in the activated catalyst is highly similar. EXAFS fitting shows that Fe is surrounded by ~ 6 O in the first shell and the Fe-Ni/Fe path in the second shell has a coordination number of ~ 2 (Supplementary Fig. 16c, d and Supplementary Table 2). The apparent Fe-Ni/Fe distance (~ 2.85 Å) from the Fe K-edge EXAFS fitting result is similar to that obtained from the Ni K-edge EXAFS (Ni-Fe distance is ~ 2.83 Å; Supplementary Table 2). A proposed formation process of Ni-Fe_2 complex catalyst is illustrated in Fig. 2g, with the atomic structure of each model being confirmed by XANES simulations (Supplementary Figs. 21–23). However, as it is difficult to distinguish Fe and Ni from each other by EXAFS fitting, the presence of Ni_3 and $\text{Ni}_2\text{-Fe}$ structures (Supplementary

Figs. 24 and 25), which could be formed through a dissolution and re-deposition process, is possible.

Theoretical understanding of the dynamic OER mechanism

We employed DFT combined AIMD simulations to gain deep atomistic insights into the dynamic nature of the Ni-Fe_2 electrocatalyst in the OER process. As depicted in Supplementary Fig. 26, Pourbaix diagram suggests reasonable stability of the proposed Ni-Fe_2 model. The OER Gibbs free energy diagram on the Ni-Fe_2 model shows that adsorption of OH^- on the Fe active site is favorable with an exothermic reaction energy of -0.22 eV, benefiting from the intramolecular hydrogen bond stabilization (Fig. 3a). Notably, a fast irreversible intramolecular proton transfer occurs from $\text{Fe}^{\text{IV}}\text{OH}$ to $\text{Ni}^{\text{IV}}\text{OH}$, resulting in the generation of $\text{Ni}^{\text{IV}}\text{OH}_2$ and $\text{Fe}^{\text{IV}}\text{O}$. Simultaneously, the formed water molecule is rapidly desorbed within a short timescale less than 5 ps, exposing the Ni site for the next catalytic cycle. These observations are supported by AIMD simulation with fully explicit solvation shells (Fig. 3b). The spontaneous intramolecular proton transfer is further confirmed by the

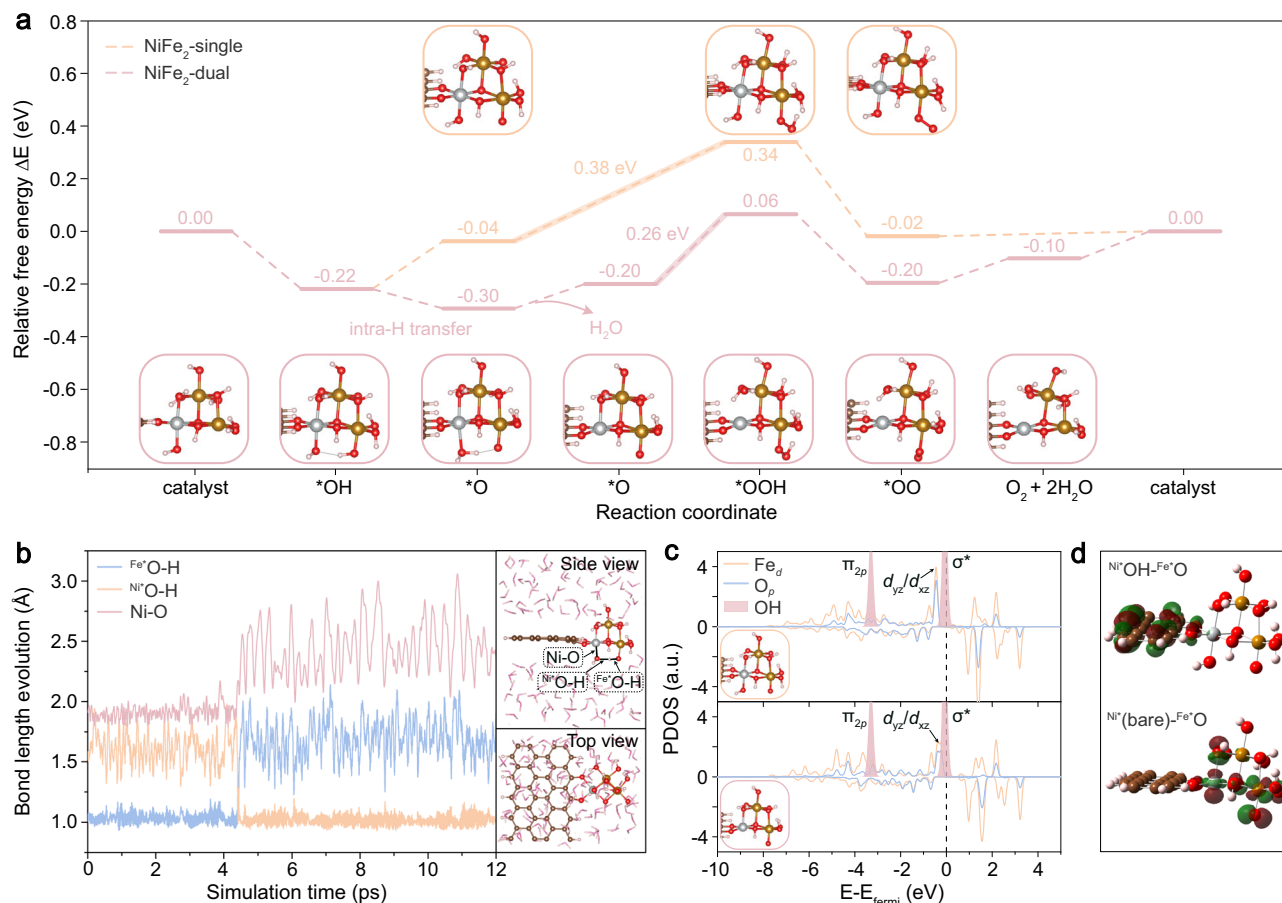


Fig. 3 | Theoretical investigation of the dynamic OER mechanism. **a** Relative free energy diagram of OER over Ni-Fe₂ triple-atom sites in alkaline media at the equilibrium potential of 1.23 V. Insets show the corresponding atomic structures.

b Evolution of Fe⁺O-H, Ni⁺O-H, and Ni-O bond lengths during the AIMD simulation on Ni⁺OH-Fe⁺O model. The insets are the side and top views of the initial state with full explicit solvation shells in the AIMD trajectories.

c PDOS analysis of Fe 3d, O 2p, and OH orbitals for OH transfer in the Ni⁺OH-Fe⁺O and Ni⁺(bare)-Fe⁺O models. Insets show the corresponding atomic structures.

d Calculated electron density distribution of the LUMOs of Ni⁺OH-Fe⁺O and Ni⁺(bare)-Fe⁺O. Red and green regions represent positive and negative signs of the wave function, respectively. Silver, gold, brown, red, and white balls represent Ni, Fe, C, O, and H atoms, respectively.

negligible proton transfer barrier and O Bader or Mulliken charge analysis; in particular, Ni⁺OH exhibits a stronger oxidation ability compared to Fe⁺OH, enabling it to seize proton from Fe⁺OH (Supplementary Figs. 27–29). On the other hand, the pre-equilibrium step (PES) could involve an intermolecular OH transfer on the single Fe⁺OH site to yield Fe⁺O with a free energy of -0.04 eV (Fig. 3a). The rate-determining step (RDS) for both the single- and dual-site reaction mechanisms are intermolecular OH attack, which experience positive reaction energies of 0.38 eV and 0.26 eV, respectively. This leads to the theoretical overpotential for driving the OER processes following the dual-site reaction mechanism being as low as 260 mV. The intramolecular proton transfer from Fe⁺OH to Ni⁺OH markedly facilitates the RDS due to the dynamic coordination of Ni site, revealing the correlation between the coordination structure and OER performance.

Given that the RDS of OER for both single- and dual-site mechanisms correlate with the formation of *OOH, the intrinsic electronic origin of the reactivity for Ni⁺OH-Fe⁺O and Ni⁺(bare)-Fe⁺O was explored. The orbital interactions between Fe⁺O and OH are illustrated in Fig. 3c. The comparison of projected density of states (PDOS) with and without OH on the Ni site uncovers that the exclusion of OH raises d_{yz}/d_{xz} orbitals of Fe near the Fermi level (Supplementary Fig. 30), exhibiting comparably larger overlaps with σ^* orbital of OH. Furthermore, Kohn–Sham molecular orbital analysis reveals that the lowest unoccupied molecular orbital (LUMO) of Ni⁺(bare)-Fe⁺O is mainly located on the Ni-Fe₂ active region while that of Ni⁺OH-Fe⁺O is completely

contributed by graphene matrix (Fig. 3d). Ni⁺(bare)-Fe⁺O exhibits a narrower highest occupied molecular orbital (HOMO)–LUMO gap of 0.99 eV than that of Ni⁺OH-Fe⁺O (2.24 eV) and thus improving reactivity (Supplementary Fig. 31)⁴⁵. Besides, Fe=O bond orders in Ni-Fe₂ molecules show that the introduction of OH on the Ni site strengthens the Fe=O bond order from 1.63 to 1.78 (Supplementary Table 3), indicating that the Fe=O double bond in Ni⁺(bare)-Fe⁺O is easier to be broken to form Ni⁺(bare)-Fe⁺OOH. It is worth noting that Ni⁺OH₂-Fe⁺O presents a similar electronic configuration to that of Ni⁺(bare)-Fe⁺O, with a HOMO–LUMO gap of 1.04 eV (Supplementary Fig. 31). However, the reaction energy of Ni⁺OH₂-Fe⁺O was calculated to be as high as 0.45 eV (Supplementary Fig. 32), further corroborating the significance of the dynamic coordination of Ni site. In addition, we have also investigated the OER mechanism on two Fe sites of Ni-Fe₂, Ni site of Ni-Fe₂, Ni single-atom, and Ni-Fe₁ double-atom models, but the reaction energies were determined to be considerably unfavorable (Supplementary Figs. 33–37 and Supplementary Table 4). Notably, the calculated reaction energies for the Ni₃, Fe₃, and Ni₂-Fe models are also higher than that for the Ni-Fe₂ model (Supplementary Figs. 38–40), indicating that Ni-Fe₂ could potentially be the major active species in Ni-Fe molecular complex for OER. Moreover, we have drawn a LSR using Ni single-atom, Ni or Fe single site of Ni-Fe₂, and Ni-Fe₁ double-atom as reference models. As shown in Supplementary Fig. 41, the free energy difference of *OOH and *OH on NiFe₂ dual-site model is 2.74 eV, notably lower than that of 3.14 eV for reference models under the

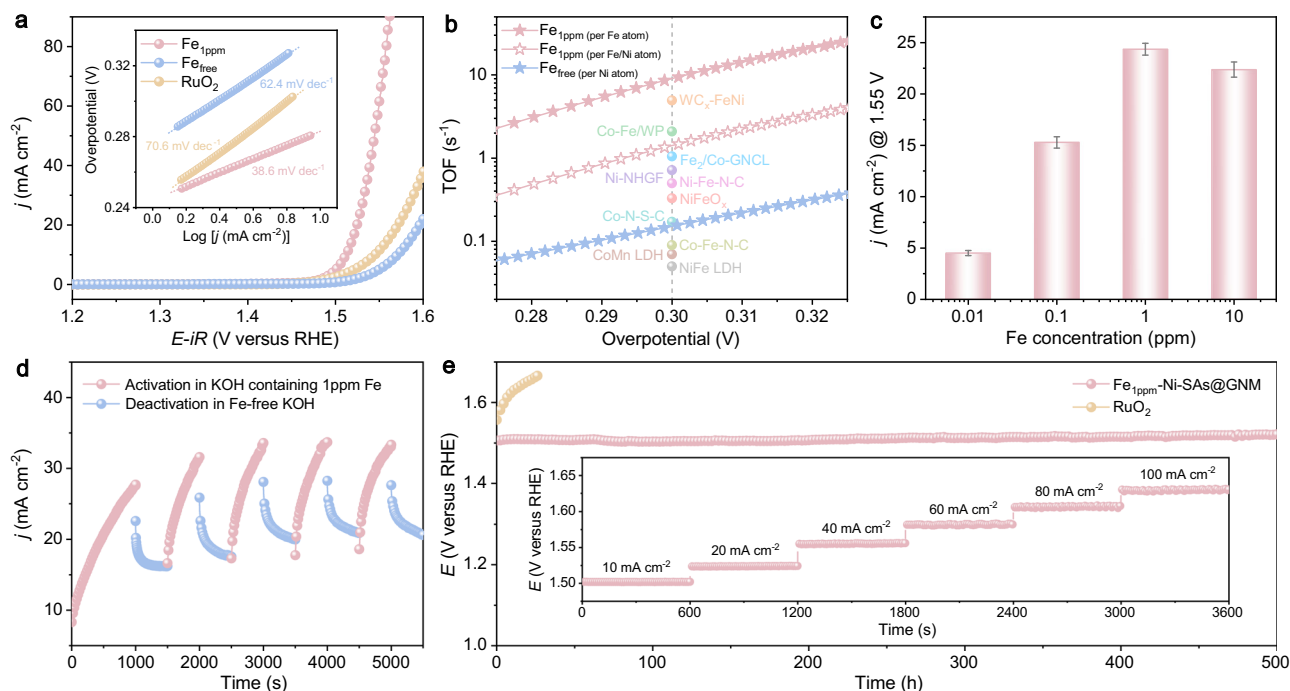


Fig. 4 | OER performance. **a** LSV curves of Fe_{1ppm}-Ni-SAs@GNM, Fe_{free}-Ni-SAs@GNM, and commercial RuO₂ catalysts with *iR*-correction, where *R* was measured to be -4.3Ω . Inset is the corresponding Tafel plots. **b** Potential dependent TOFs of Fe_{1ppm}-Ni-SAs@GNM and Fe_{free}-Ni-SAs@GNM in comparison with various state-of-the-art OER catalysts reported in the literature (Supplementary Table 5). **c** Effect of Fe concentration in the electrolyte on OER activity. The error bars are

means \pm standard deviation (3 replicates). **d** Repetitive chronoamperometric measurements of Fe_{1ppm}-Ni-SAs@GNM between 1 M KOH containing 1 ppm Fe and Fe-free KOH electrolyte at 1.6 V versus RHE. **e** Long-term chronopotentiometry tests of Fe_{1ppm}-Ni-SAs@GNM in comparison with RuO₂ at 10 mA cm⁻². Inset depicts the multi-current electrochemical process.

restriction of scaling relation. In short, these theoretical studies discover an unconventional dynamic dual-site-cooperated OER mechanism (Supplementary Fig. 42). The dynamic evolution of the Ni site in Ni-Fe₂ model can effectively regulate the electronic structure of the adjacent Fe active centre during the OER cycle, and simultaneously lower the free energies of O–H bond cleavage and *OOH formation, which eventually breaks the LSRs in OER.

OER electrocatalysis

Considering the favorable OER catalytic pathway of our designed Ni-Fe₂ molecular complex catalyst, we investigated the actual electrocatalytic OER performance. Figure 4a shows the linear sweep voltammetry (LSV) curves and the corresponding Tafel plots. The Fe_{1ppm}-Ni-SAs@GNM catalyst exhibits an overpotential of only 282 mV at 10 mA cm⁻² and a Tafel slope of 38.6 mV dec⁻¹, which outperforms the commercial RuO₂ (315 mV, 70.6 mV dec⁻¹) and Fe_{free}-Ni-SAs@GNM (341 mV, 62.4 mV dec⁻¹). LSV curves without *iR*-correction are presented in Supplementary Fig. 43 as a reference. Electrochemically active surface area (ECSA) normalized OER activity of Fe_{1ppm}-Ni-SAs@GNM is also higher than that of Fe_{free}-Ni-SAs@GNM, implying an increase of intrinsic OER activity due to Fe incorporation (Supplementary Fig. 44). Consistently, the electrochemical impedance of Fe_{1ppm}-Ni-SAs@GNM is lower (Supplementary Fig. 45). Besides, the required overpotential to reach 10 mA cm⁻² can be further decreased to 263 mV when decorating Fe_{1ppm}-Ni-SAs@GNM onto a 3D carbon cloth support (Supplementary Fig. 46). In addition, the Fe_{1ppm}-Ni-SAs@GNM demonstrates better OER activity in comparison to state-of-the-art NiFe hydroxide (Supplementary Fig. 47).

Based on rotating ring-disk electrode (RRDE) measurement, Fe_{1ppm}-Ni-SAs@GNM undertakes a four-electron water oxidation pathway (i.e., $4\text{OH}^- \rightarrow 2\text{H}_2\text{O} + \text{O}_2 + 4\text{e}^-$, Supplementary Fig. 48a) with a high O₂ Faradaic efficiency (FE) of 99.7% (Supplementary Fig. 48b). To

further evaluate the intrinsic activity of the catalyst, the turnover frequency (TOF) was calculated on the basis of ICP-OES and plotted against the overpotential (Fig. 4b). Based on Fe content, a notable TOF value of 9.2 s⁻¹ is achieved over Fe_{1ppm}-Ni-SAs@GNM at an overpotential of 300 mV, which is much higher than that of Fe_{free}-Ni-SAs@GNM (0.15 s⁻¹) and the state-of-the-art OER catalysts reported in the literature (Supplementary Table 5). Based on the total Fe and Ni contents, the TOF is still outstanding. Notably, the specific mass activity of Fe_{1ppm}-Ni-SAs@GNM was also calculated to be as high as 9.1 A mg_{NiFe}⁻¹ at the overpotential of 300 mV, which is more than 9 times higher than that of Fe_{free}-Ni-SAs@GNM (1.0 A mg_{Ni}⁻¹; Supplementary Fig. 49). As shown in Fig. 4c, the OER activity of Fe_{xppm}-Ni-SAs@GNM improves with increasing Fe concentration in the electrolyte up to 1 ppm, but deteriorates at a higher Fe concentration (10 ppm) due to formation of Fe hydroxide precipitates. The OER activity of Fe_{1ppm}-Ni-SAs@GNM also gradually increases with extended activation time (Supplementary Fig. 50). These results demonstrate that incorporation of Fe could be roughly controlled by adjusting Fe concentration in KOH and the activation time. On the other hand, the presence of 1 ppm Fe in the electrolyte had no significant impact on the OER activity of Ni-free reduced GO (Supplementary Fig. 51). Interestingly, the incorporation of Fe ions into Ni-SAs@GNM is reversible. When Fe_{1ppm}-Ni-SAs@GNM was subjected to electrolysis in Fe-free KOH electrolyte, the OER activity gradually decreased. But the activity could be recovered through reactivation in KOH electrolyte containing 1 ppm Fe ions, suggesting that the adsorption and desorption of Fe ions is a dynamic equilibrium process (Fig. 4d and Supplementary Fig. 52). The dynamic Fe exchange during OER agrees with a previous report⁴⁶. As depicted in Fig. 4e, the long-term OER stability of Fe_{1ppm}-Ni-SAs@GNM is notable. Specifically, the overpotential at a constant OER current density of 10 mA cm⁻² only slightly increased by 15 mV after 500 h of continuous electrolysis. By contrast, rapid decay was

observed in the activity of the commercial RuO_2 . Aberration-corrected HAADF-STEM shows that the Ni and Fe atoms in $\text{Fe}_{1\text{ppm}}\text{-Ni-SAs@GNM}$ still nearly remain atomic dispersion even after 500 h of operation (Supplementary Fig. 53). Furthermore, the potential quickly stabilizes upon step-wise increase of OER current (Fig. 4d inset), indicating effective mass transport on the electrode surface during OER (inward diffusion of OH^- and outward diffusion of oxygen bubbles), owing to the 2D nanomesh structure¹⁴. The practical viability of $\text{Fe}_{1\text{ppm}}\text{-Ni-SAs@GNM}$ was demonstrated by the good performance of the overall water-splitting cell and the rechargeable Zn-air battery (Supplementary Figs. 54 and 55). In addition, Co-SAs@GNM (changing metal centre) was synthesized following a similar procedure as Ni-SAs@GNM , and its OER activity was also largely improved after activation in KOH containing 1 ppm Fe ions (Supplementary Fig. 56), indicating the possible formation of Co-Fe active units and possibility to construct various dynamic molecular catalysts.

Electrokinetic investigations

Electrokinetic studies were further performed to comprehend the catalytic mechanism from an experimental perspective. We employed a quasi-equilibrium model to describe the OER kinetics, where the key steps include a PES followed by a RDS¹⁵. Firstly, the OER activities at different concentrations of OH^- were measured based on LSV at the normal hydrogen electrode (NHE) scale, and the catalytic activity shows an increase with increasing OH^- concentration (Fig. 5a and Supplementary Fig. 57a). Additionally, $\text{Fe}_{1\text{ppm}}\text{-Ni-SAs@GNM}$ also displays pH-dependent OER activities on the RHE scale, suggesting that the proton transfer and the electron transfer are non-concerted during the OER (Supplementary Fig. 57b)^{7,47}. As shown in Fig. 5b, $\text{Fe}_{1\text{ppm}}\text{-Ni-SAs@GNM}$ exhibits a similar Tafel slope of $40 \pm 1 \text{ mV dec}^{-1}$ in 0.1 to 2 M KOH, implying that OER over $\text{Fe}_{1\text{ppm}}\text{-Ni-SAs@GNM}$ proceeds with a PES involving one-electron transfer, followed by a RDS involving another electron transfer

(Supplementary Table 6)^{15,48}. By plotting the potentials at a current density of 1 mA cm^{-2} versus $\log [\text{OH}^-]$ (this current density was selected to minimize the influence of Tafel slope variation⁴⁹), a slope of -82.3 mV is derived (Fig. 5a inset), indicating that the catalytic activity has an approximately second-order dependence on OH^- concentration¹⁵. Consequently, the PES and RDS involve the transfer of two OH^- in total (Supplementary Table 6). CV was then performed to determine OH^- participation in the $\text{Ni}^{2+}/\text{Ni}^{3+}$ redox process (Fig. 5c). As illustrated in Fig. 5d, the reduction peak for the pre-catalytic $\text{Ni}^{2+}/\text{Ni}^{3+}$ redox couple (the oxidation peak is masked by OER current) shifts by $-107.6 \text{ mV}/\log [\text{OH}^-]$, suggesting that oxidation of Ni site prior to PES is accompanied by two OH^- transfer (Supplementary Table 6). Furthermore, deuterium (D) kinetic isotope effect (KIE) experiment was conducted to probe the possible transfer of proton/hydrogen in the RDS. The LSV of $\text{Fe}_{1\text{ppm}}\text{-Ni-SAs@GNM}$ in a 1 M KOD/ D_2O electrolyte shows a comparable current density to that in 1 M KOH/ H_2O electrolyte (Fig. 5e). By comparing the current densities in KOH and KOD at the same overpotentials, the average KIE value of $\text{Fe}_{1\text{ppm}}\text{-Ni-SAs@GNM}$ was calculated to be 1.13 ± 0.09 (nearly potential-independent), indicating a secondary KIE ($\text{KIE} < 1.5$) where proton/hydrogen transfer is absent in RDS (Fig. 5e inset and Supplementary Table 6)^{7,15,50}. Moreover, due to the stronger D-bonding relative to H-bonding network, the CV reduction peak for the pre-catalytic $\text{Ni}^{2+}/\text{Ni}^{3+}$ redox couple in KOD displays a positive shift of -26 mV compared to that in KOH (Supplementary Fig. 58), further confirming that the pre-oxidation of the Ni site is accompanied by terminating $-\text{OH}$. Additionally, we performed methanol oxidation experiments to probe the surface coverage of $^*\text{OH}$ intermediate on the catalysts (Supplementary Fig. 59). In comparison to $\text{Fe}_{\text{free}}\text{-Ni-SAs@GNM}$, $\text{Fe}_{1\text{ppm}}\text{-Ni-SAs@GNM}$ exhibits a reduced current difference and a positive shift of the onset potential for methanol oxidation, suggesting a lower surface coverage of $^*\text{OH}$ on $\text{Fe}_{1\text{ppm}}\text{-Ni-SAs@GNM}$ during OER⁵¹. This result may suggest the existence of

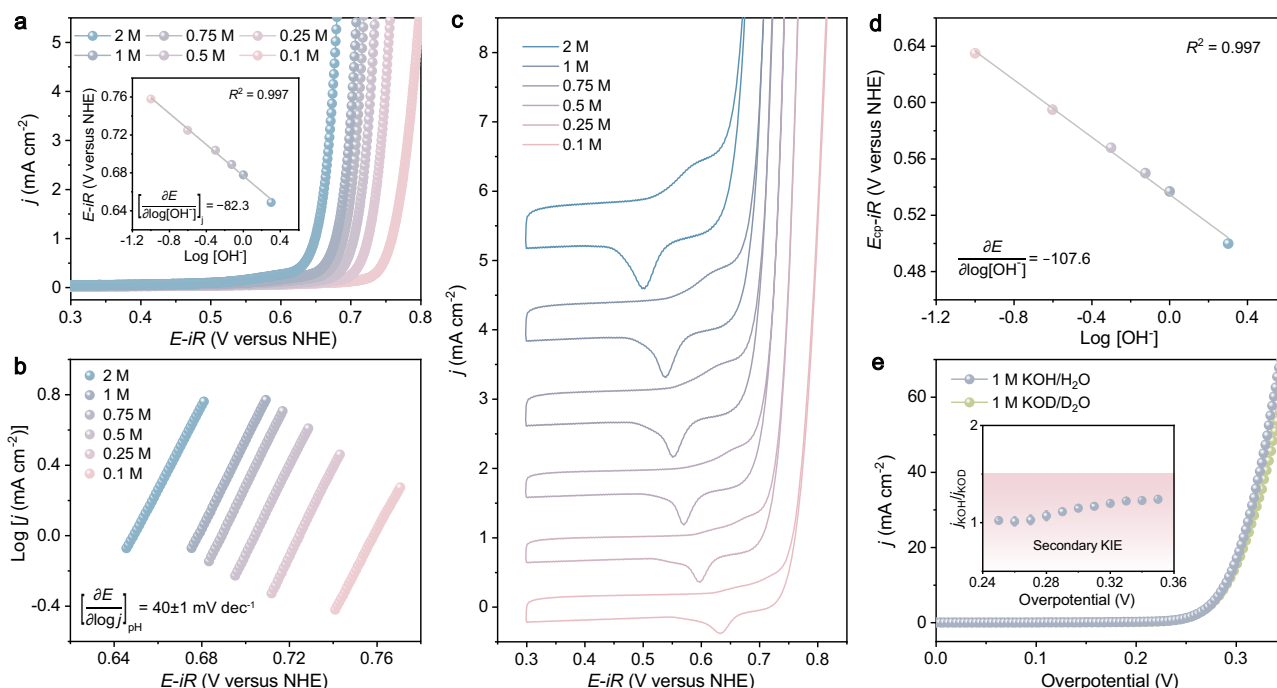


Fig. 5 | Electrokinetic investigations. **a** LSV curves of $\text{Fe}_{1\text{ppm}}\text{-Ni-SAs@GNM}$ recorded under different KOH concentration with iR -correction, where R was measured to be -28.1 , -12.3 , -6.7 , -5.2 , -4.3 , and -2.8Ω for 0.1, 0.25, 0.5, 0.75, 1, and 2 M KOH, respectively. Inset is the fitting plot of the potential at 1 mA cm^{-2} versus the logarithm of $[\text{OH}^-]$. **b** Corresponding Tafel plots derived from (a). **c** CV curves of

$\text{Fe}_{1\text{ppm}}\text{-Ni-SAs@GNM}$ recorded under different KOH concentrations with iR -correction. **d** Fitting plot of the iR -corrected reduction potential for the cathodic peak ($E_{\text{cp}}-iR$) versus the logarithm of $[\text{OH}^-]$. **e** LSV curves of $\text{Fe}_{1\text{ppm}}\text{-Ni-SAs@GNM}$ in 1 M KOH/ H_2O and KOD/ D_2O electrolytes. Inset is the KIE values versus overpotential. The error bars are means \pm standard deviation (3 replicates).

intramolecular proton transfer from $\text{Fe}^{\text{IV}}\text{OH}$ to $\text{Ni}^{\text{II}}\text{OH}$ during OER, which subsequently reduces the surface coverage of $\ast\text{OH}$.

Based on the above analyses, a possible reaction mechanism was proposed over $\text{Fe}_{\text{1ppm}}\text{-Ni-SAs@GNM}$ (Supplementary Fig. 60). Ni^{2+} is first oxidized to Ni^{3+} accompanied by the combination of two OH^- , leading to the coordination reconstruction of Ni site. Subsequently, one OH^- is adsorbed onto Fe site to initiate OER. As suggested by the evidence of Fe^{4+} from the *operando* XAFS result and AIMD simulation, the adsorbed OH undergoes deprotonation through an intramolecular proton transfer from $\text{Fe}^{3+}\text{-OH}$ to $\text{Ni}^{3+}\text{-OH}$. Consequently, $\text{Fe}^{3+}\text{-OH}$ is oxidized to $\text{Fe}^{4+}=\text{O}$, whereas $\text{Ni}^{3+}\text{-OH}$ is reduced to $\text{Ni}^{2+}\text{-H}_2\text{O}$ accompanied by desorption of H_2O . Noteworthy, this step proceeds very fast and does not involve OH^- and electron transfer; hence, the initial adsorption of OH^- on Fe site should be regarded as the PES followed by one- OH^- and one-electron transfer. Then it comes to the RDS in which one OH^- attacks on $\text{Fe}^{4+}=\text{O}$ to form $\text{Fe}^{3+}\text{-OOH}$, yielding a secondary KIE. The next step involves a proton-coupled electron transfer from $\text{Fe}^{3+}\text{-OOH}$ to $\text{Fe}^{3+}\text{-OO}^\bullet$. Finally, O_2 is released from Fe site, concomitant with the nucleophilic attack of OH^- on Ni^{2+} to generate $\text{Ni}^{3+}\text{-OH}$ for the next catalytic cycle. It is noteworthy that the proposed OER mechanism for $\text{Fe}_{\text{1ppm}}\text{-Ni-SAs@GNM}$ is consistent with theoretical prediction (Fig. 3a). Other potential reaction mechanisms, such as the lattice-oxygen-mediated mechanism, can be excluded by a tetramethylammonium cation (TMA^+) probing experiment (Supplementary Fig. 61)⁵², while the O–O coupling mechanism has been ruled out based on unfavorable thermodynamic overpotential and Tafel slope analysis (Supplementary Figs. 62 and 63). Likewise, reaction mechanism of $\text{Fe}_{\text{free}}\text{-Ni-SAs@GNM}$ is discussed in Supplementary Figs. 64 and 65, and Supplementary Table 6.

Discussion

In summary, we have reported an in situ electrochemical conversion process for directly constructing a Ni- Fe_2 molecular complex catalyst, which is confirmed by *operando* XAFS. Theoretical calculations based on this model catalyst demonstrate that the dynamic structural evolution of the Ni site induced by intramolecular proton transfer can effectively alter the electronic structure of the neighboring Fe active site, which in turn leads to the simultaneous reduction of free energy changes for O–H bond cleavage and O–O bond formation. Such dynamic dual-site cooperation observed within the catalytic cycle allows the Ni-Fe molecular complex catalyst to circumvent the oxygen evolution LSRs imposed by the conventional static AEM. As a result, the catalyst presents TOF values that surpass most of the state-of-the-art catalysts reported thus far. Furthermore, electrokinetic investigations provide experimental evidence supporting the mechanism. This work not only advances the development of molecular water oxidation catalysts, but also provides an unconventional paradigm for breaking the universal scaling relations in chemical reactions involving multiple intermediates.

Methods

Chemicals and materials

Iron nitrate nonahydrate ($\text{Fe}(\text{NO}_3)_3 \cdot 9\text{H}_2\text{O}$, $\geq 99.95\%$), nickel nitrate hexahydrate ($\text{Ni}(\text{NO}_3)_2 \cdot 6\text{H}_2\text{O}$, 99.999%), zinc acetate dihydrate ($\text{Zn}(\text{CH}_3\text{COO})_2 \cdot 2\text{H}_2\text{O}$, $\geq 98\%$), potassium hydroxide (KOH, 90%), hydrochloric acid (HCl, 37%), methanol (CH_3OH , $\geq 99.9\%$), isopropanol ($(\text{CH}_3)_2\text{CHOH}$, $\geq 99.5\%$), tetramethylammonium hydroxide (TMAOH, 25 wt% in H_2O), potassium deuterioxide (KOD, 40 wt% in D_2O , 98 atom% D), nafion 117 solution ($\sim 5\%$ in a mixture of lower aliphatic alcohols and water), Pt/C (20 wt% loading on graphitized carbon), and ruthenium oxide (RuO_2 , 99.9%) were purchased from Sigma-Aldrich. Deuterium oxide (D_2O , 99.9 atom% D) was purchased from Cambridge Isotope Laboratories, Inc. All chemicals were used as received without further purification, unless noted otherwise. Ni and Co vessel (50 mL) was purchased from Kunshan Electronic Co., Ltd. All aqueous solutions

were prepared using deionized (DI) water with a resistivity of 18.2 M Ω cm at room temperature.

Synthesis of Ni-SAs@GNM

GO was first synthesized using a modified Hummers' method⁵³. Then, 40 mL of GO aqueous suspension (3 mg mL⁻¹, pH 5) was sealed in a Ni vessel and heated at 80 °C for 48 h. After cooling to room temperature, the resulting hydrogel-like assembly was repeatedly rinsed with DI water, followed by freeze drying to obtain $\text{Ni}(\text{OH})_2/\text{graphene}$ aerogel. Subsequently, the aerogel was annealed at 700 °C for 2 h under an Ar atmosphere (100 sccm), with a heating rate of 5 °C min⁻¹. Finally, the product was leached at 80 °C in 2 M HCl for 24 h and thoroughly washed with DI water. Co-SAs@GNM was synthesized using the same procedure, except using Co vessel as the reactor. The reduced GO was synthesized by pyrolyzing GO at 700 °C for 2 h under an Ar atmosphere.

KOH electrolyte purification

1 M KOH solutions made from commercial KOH flakes (90%) were estimated to contain ~ 0.12 ppm Fe by ICP-OES measurements. Fe impurities in such commercial KOH solutions can be removed by treating with $\text{Ni}(\text{OH})_2$ ³². Briefly, 2 g of $\text{Ni}(\text{NO}_3)_2 \cdot 6\text{H}_2\text{O}$ was dissolved in 5 mL of DI water. Then 20 mL of 1 M KOH was added to induce the precipitation of $\text{Ni}(\text{OH})_2$ solids, followed by washing with DI water and 1 M KOH successively. The purification process involves dispersing $\text{Ni}(\text{OH})_2$ in 50 mL of 1 M KOH solution, mechanically agitated overnight, followed by centrifugation. Consequently, the Fe content in purified 1 M KOH was below or at the detection limit of ICP-OES (< 3 ppb). Purified 1 M KOH (pH = 13.6 ± 0.1) was stored in a polypropylene beaker before usage.

Synthesis of Ni-Fe molecular complex catalyst

Ni-Fe molecular complex catalyst was prepared by electrochemical activation of Ni-SAs@GNM in purified KOH containing 1 ppm Fe, using a standard three-electrode system (CHI 760E, CH Instruments) under ambient conditions, with a Pt wire as the counter electrode and a Hg/HgO electrode (in 1 M KOH) as the reference electrode. To prepare working electrode, 5 mg of Ni-SAs@GNM powders were dispersed into an aqueous solution containing 0.97 mL isopropanol and 30 μL Nafion solution (5 wt%) under sonication for 1 h. Then 12 or 15 μL of such ink was uniformly dropped onto a L-type glassy carbon electrode (5 mm in diameter) or a carbon cloth (WOS 1002, $0.5 \times 0.5 \text{ cm}^2$), respectively (catalyst loading: 0.3 mg cm⁻²), and allowed to dry at room temperature. The electrolyte was prepared by adding 220 μL of 1 mg mL⁻¹ $\text{Fe}(\text{NO}_3)_3 \cdot 9\text{H}_2\text{O}$ solution into 30 mL of purified KOH solution under vigorous stirring. The freshly prepared electrolyte was promptly utilized. Electrochemical activation was then performed using cyclic voltammetry (CV) between 1.1 and 1.65 V versus RHE at the scan rate of 50 mV s⁻¹. Additionally, anodic chronopotentiometry with a current density of 5 mA cm⁻² or chronoamperometry at 1.6 V versus RHE can also be employed for activation. Co-Fe molecular complex can be synthesized using the same procedure, except using Co-SAs@GNM as the pre-catalyst.

Material characterization

The crystal structure was analyzed using powder XRD with Cu K α irradiation ($\lambda = 1.5406 \text{ \AA}$) on a Bruker D2 Phaser. Morphology was examined with field-emission SEM (JEOL JSM-6700) and field-emission TEM (JEOL JEM-2100F). Atomic resolution imaging was performed with an aberration-corrected HAADF-STEM (JEOL JEM-ARM200F) at 80 kV. Chemical composition analysis was carried out by XPS on a Thermo Scientific ESCALAB Xi⁺ with a monochromatic Al K α source ($h\nu = 1486.6 \text{ eV}$), using the C 1s peak at 284.8 eV for binding energy calibration. Raman spectra were recorded on a Renishaw spectrometer with a 514 nm laser source. UV-vis adsorption

spectra were recorded on a UV-1800 Shimadzu spectrophotometer. N₂ adsorption–desorption isothermals were measured at 77 K on a Micromeritics ASAP 2020 analyzer. The Brunauer-Emmett-Teller (BET) and Barrett-Joyner-Halenda (BJH) methods were used to calculate the specific surface area and pore size distribution, respectively. The metal contents in the samples and electrolytes were determined by ICP-OES (Agilent 720ES). First, the samples were hydrothermally treated in the mixture of concentrated H₂SO₄, HNO₃, and HCl with volume ratio of 1:1:2 at 180 °C for 24 h. The resultant solution was then diluted with DI water for ICP-OES analysis.

XAS characterization

Ex situ and operando Ni/Fe K-edge XANES and EXAFS experiments were carried out at the XAFS for catalysis (XAFCA) beamline⁵⁴ of Singapore Synchrotron Light Source (SSLS) in fluorescence mode. Energy calibration was performed using Ni/Fe foil as the standard. For ex situ analysis, solid powder samples were deposited on carbon paper, while operando measurements employed a customized electrochemical cell with continuous flow of 1 M KOH containing 1 ppm Fe electrolyte. The catalyst ink was drop-casted onto carbon paper (1 mg cm⁻²) taped with Kapton polyimide film on the back as the working electrode. A graphite rod served as the counter electrode, while an Ag/AgCl electrode (in saturated KCl) was used as the reference electrode. XAFS data were recorded under chronopotentiometric mode at a current density of 5 mA cm⁻² during electrochemical activation. EXAFS data processing and analysis were completed using Athena and Artemis software within the DEMETER package⁵⁵. Ni L_{2,3}-edge XAS data were collected at the SSLS Soft X-ray-ultraviolet (SUV) beamline. Fe/Ni ratio was estimated using the edge step (ES) of unnormalized Fe and Ni K-edge XANES spectra, calculated as Fe/Ni ratio = ES_{Fe@sample}/ES_{Ni@sample}. It is worth noting that the difference in fluorescence yield between Ni and Fe atoms was not considered in this estimation, as their values are quite close. Alternatively, Fe/Ni ratio can also be determined by SXRF measurements with a probe area of 2 mm (horizontal) × 1 mm (vertical).

Electrochemical measurements

All electrochemical measurements were conducted under ambient conditions on a CHI 760E electrochemical workstation (CH Instruments) using a standard three-electrode setup, with a working electrode of either a glassy carbon electrode or carbon cloth coated with the synthesized catalysts, a counter electrode of Pt wire, and a Hg/HgO reference electrode. A polypropylene-based cell (50 mL) was utilized to minimize contamination from glassware in alkaline solutions. Prior to each measurement, the cell and Pt wire counter electrode were cleaned thoroughly with 1 M HCl followed by DI water to prevent cross-contamination. The reference electrode was calibrated against an unused Hg/HgO electrode stored in 1 M KOH solution. All electrochemical measurements were conducted in purified KOH electrolyte or KOH with a defined concentration of Fe ions (0.01, 0.1, 1, and 10 ppm). The electrolyte was continuously stirred by a magnetic bar to prevent O₂ bubbles from accumulating on the electrode surface during OER. Polarization curves were recorded using LSV at a scan rate of 5 mV s⁻¹ with *iR*-correction, where *R* was measured to be ~4.3 Ω. All potentials were referenced to the RHE scale by *E* (versus RHE) = *E*(Hg/HgO) + 0.059 × pH + 0.098 V, unless otherwise specified. To explore the dynamic behavior of the catalyst, repetitive chronoamperometric measurements were conducted between 1 M KOH containing 1 ppm Fe and purified KOH electrolyte at 1.6 V versus RHE. Electrochemical impedance spectroscopy (EIS) was carried out at 1.55 V versus RHE in the frequency range from 100 kHz to 1 Hz with an amplitude of 10 mV.

Tafel plots are commonly used to describe the kinetics of electron transfer reactions⁴⁸. The Tafel equation relates the Tafel slope to the

exchange current density as follows:

$$\eta = -\frac{2.303RT}{\alpha F} \times \log i_0 + \frac{2.303RT}{(\alpha + n)F} \times \log i \quad (1)$$

In this equation, the Tafel slope is defined as 2.303RT/(α + n)F, where *i*₀ represents the exchange current density, *R* is the universal gas constant, *T* is the absolute temperature, *F* is the Faraday constant, *n* refers to the number of electrons transferred before RDS, and α is the charge transfer coefficient).

ECSA was estimated from the electrochemical double-layer capacitance (*C*_{dl}) using the following equations:

$$C_{dl} = \frac{j_a - j_c}{2 \times \nu} \quad (2)$$

where *j*_a and *j*_c represent the charging and discharging current densities, respectively; ν is the scan rate. *C*_{dl} was derived from CV curves recorded at various scan rates (10, 20, 40, 60, 80, and 100 mV s⁻¹) within the potential window of 1.05–1.15 V versus RHE without Faradic current. The difference between *j*_a and *j*_c at 1.1 V versus RHE was used for calculation.

$$ECSA = \frac{C_{dl}}{C_s} \times A \quad (3)$$

where *C*_s is the specific capacitance of the sample and *A* is the geometric area of the electrode. Here, a general value of *C*_s = 0.04 mF cm⁻² in 1 M KOH was adopted⁵⁶.

RRDE measurements were conducted to determine the electron transfer number (*n*) and peroxide yield (%HO₂⁻) during OER through the following equations:

$$n = 4 \times \frac{I_d}{I_d + I_r/N} \quad (4)$$

$$\%HO_2^- = 200 \times \frac{I_r/N}{I_d + I_r/N} \quad (5)$$

where *I*_d is the current from the disk electrode, *I*_r is the current from the ring electrode, and *N* is the current collection efficiency of the Pt ring (0.37). The working electrode was scanned at 5 mV s⁻¹ with a rotating speed of 1600 rpm, the Pt ring potential was fixed at 1.5 V versus RHE.

FE was calculated using the following equation:

$$FE = \frac{I_r}{I_d \times N} \quad (6)$$

where *I*_d was held constant at a small level of 200 μA. Meanwhile, the Pt-ring potential was fixed at 0.4 V versus RHE to detect the reduction of generated O₂.

The TOF was evaluated by the following equation:

$$TOF = \frac{J \times A}{4 \times m \times F} \quad (7)$$

where *J* is the anodic current density, *A* is the geometric area of the electrode, *m* is the mole number of active sites on the electrode, and *F* is Faraday constant (96,485 C mol⁻¹).

pH-dependence experiments were conducted using KOH solutions with different concentrations (0.1, 0.25, 0.5, 0.75, 1, and 2 M). The measured solution resistances of 0.1, 0.25, 0.5, 0.75, 1, and 2 M KOH were ~28.1, ~12.3, ~6.7, ~5.2, ~4.3, and ~2.8 Ω, respectively. LSV and CV curves were recorded for each KOH solution. The relationship between

the potential (versus NHE) at a constant current and the concentration of OH[−] ($(\partial E/\partial \log[\text{OH}^-])_j$) was determined by calculating the potential at a constant current density of 1 mA cm^{−2} and log [OH[−]], followed by linear fitting¹⁵. Tafel plots were extracted from the LSV curves and linear fitted to yield $(\partial E/\partial \log j)_{\text{pH}}$. The reaction order based on OH[−] ($(\partial j/\partial \log[\text{OH}^-])_E$) was then determined using the following equation^{15,50}:

$$\left[\frac{\partial \log j}{\partial \log[\text{OH}^-]} \right]_E = - \frac{\left[\frac{\partial E}{\partial \log[\text{OH}^-]} \right]_j}{\left[\frac{\partial E}{\partial \log j} \right]_{\text{pH}}} \quad (8)$$

Hydrogen/deuterium (H/D) isotope experiments were performed using LSV in 1 M KOH aqueous solution and 1 M KOD in D₂O. The latter was prepared by diluting 40 wt% KOD with D₂O. The corresponding current densities at a given overpotential were denoted as j_{KOH} and j_{KOD} , respectively. The kinetic isotope effect (KIE) was defined using the following equation:

$$\text{KIE} = \left[\frac{j_{\text{KOH}}}{j_{\text{KOD}}} \right]_{\eta} \quad (9)$$

The overpotential in KOH (η_{KOH}) can be corrected by following equation:

$$\eta_{\text{KOH}} = E(\text{Hg}/\text{HgO}) + E(\text{Hg}/\text{HgO}, \text{NHE}) + 0.059 \times \text{pH} - 1.229 V_{\text{RHE}} \quad (10)$$

where $E(\text{Hg}/\text{HgO})$ refers to the potential measured using the Hg/HgO reference electrode, and $E(\text{Hg}/\text{HgO}, \text{NHE})$ is the equilibrium potential of the Hg/HgO couple on the NHE scale (0.098 V).

Since the equilibrium potentials for D₂/D⁺ and O₂/D₂O redox couples differ from those of H₂/H⁺ and O₂/H₂O redox couples, overpotentials should be corrected to the RDE (reversible “deuterium” electrode) scale. The different free energies of formation for H₂O (−237.18 kJ mol^{−1}) versus D₂O (−243.49 kJ mol^{−1}) result in different equilibrium potentials of 1.229 V_{RHE} and 1.262 V_{RDE} for water oxidation⁵⁷. As known, pK_{D₂O} = pOD + pD = 14.87; pK_{H₂O} = pOH + pH = 14⁵⁸. Given that the concentration of OH[−] and OD[−] are identical in 1 M KOH and 1 M KOD solutions (pOD ≈ pD), the pD of KOD can be calculated by adding 0.87 to the pH of KOH at the same concentration. Consequently, the overpotential in KOD (η_{KOD}) can be corrected by following equation:

$$\eta_{\text{KOD}} = E(\text{Hg}/\text{HgO}) + E(\text{Hg}/\text{HgO}, \text{NDE}) + 0.059 \times (\text{pH} + 0.87) - 1.262 V_{\text{RDE}} \quad (11)$$

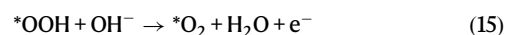
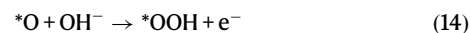
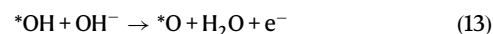
where $E(\text{Hg}/\text{HgO}, \text{NDE})$ represents the equilibrium potential of the Hg/HgO couple on the NDE (normal “deuterium” electrode) scale. The equilibrium potential for the D₂/D⁺ couple (−0.013 V) differs from that of the H₂/H⁺ couple (0 V), indicating a difference of −0.013 V between the NDE and NHE scales⁵⁷. Therefore, $E(\text{Hg}/\text{HgO}, \text{NDE})$ is calculated as (0.098–0.013) V.

Computational details

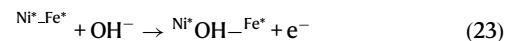
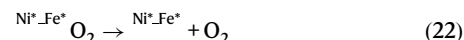
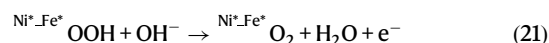
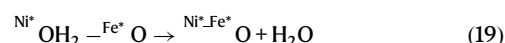
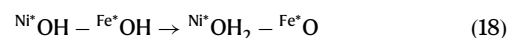
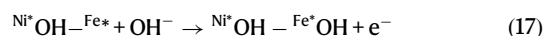
DFT calculations were performed using the Vienna Ab-initio Simulation Package program^{59–61}. The electron-core interaction was described by the projector augmented wave method. The exchange–correlation energy was described by the Perdew–Burke–Ernzerhof functional within the generalized gradient approximation⁶². A plane-wave cutoff energy of 400 eV was applied for expanding the Kohn–Sham wave functions. Sampling of the Brillouin zone was carried out using a 1 × 1 × 1 Monkhorst–Pack k-point grid, while electronic occupancies were determined using Gaussian smearing with a width of 0.05 eV. Additional calculations for Kohn–Sham molecular orbitals, Mayer bond orders, and atomic charges were performed using the Gaussian

16 program⁶³. The Ni and Fe transition metals were loaded on the edge of 4 × 2 graphene unit cells with supercell dimensions of 12.3 × 17.0 × 20.00 Å³.

The conventional single-site OER reaction pathway in alkaline media can be summarized as follows:



While the dual-site OER reaction pathway is:



where Ni* and Fe* denote the active sites of Ni and Fe, respectively.

Following the computational hydrogen electrode (CHE) model⁶⁴, the reaction free energy (ΔG) for each step is calculated as follows:

$$\Delta G = \Delta E + \Delta \text{ZPE} - T\Delta S - |e|U \quad (24)$$

where ΔE is the reaction energy from DFT calculations, ΔZPE is the change in zero-point energy, T is the temperature of 298.15 K, ΔS is the change in entropy, e is the transferred charge, and U is the applied potential. The free energy of (H⁺ + e[−]) is equal to that of 1/2 H₂. The calculated values are shown in Supplementary Table 7. The free energy of O₂ was derived as $G_{\text{O}_2} = 2G_{\text{H}_2\text{O}} - 2G_{\text{H}_2} + 4.92$.

All AIMD simulations were conducted by employing the CP2K package⁶⁵. The simulations were sampled by the canonical (NVT) ensemble using Nose–Hoover thermostats^{66,67} with a finite temperature of 300 K for 12 ps. The model included 111 water molecules, resulting in an average density of ~1 g/cm³ to replicate the solvent environment. Free energy profiles for intramolecular H transfer were calculated by integrating the potential of mean force along predefined reaction coordinates, represented by collective variables (CVs)⁶⁸. Each constrained MD simulation began with a 1 ps equilibration followed by a 1 ps production to collect data for mean force calculations.

The atomic coordinates of the optimized models, and the initial and final configurations in AIMD simulations are provided in Supplementary Data 1.

Data availability

We declare that all data supporting the findings of this study are available in the paper and Supplementary Information. Source data file has been deposited in Figshare under accession code (<https://doi.org/10.6084/m9.figshare.27086794>)⁶⁹.

References

- Abild-Pedersen, F. et al. Scaling properties of adsorption energies for hydrogen-containing molecules on transition-metal surfaces. *Phys. Rev. Lett.* **99**, 016105 (2007).
- Mehta, P. et al. Overcoming ammonia synthesis scaling relations with plasma-enabled catalysis. *Nat. Catal.* **1**, 269–275 (2018).
- Vojvodic, A. & Nørskov, J. K. New design paradigm for heterogeneous catalysts. *Natl. Sci. Rev.* **2**, 140–149 (2015).
- Greeley, J. Theoretical heterogeneous catalysis: scaling relationships and computational catalyst design. *Annu. Rev. Chem. Biomol. Eng.* **7**, 605–635 (2016).
- Suen, N. T. et al. Electrocatalysis for the oxygen evolution reaction: recent development and future perspectives. *Chem. Soc. Rev.* **46**, 337–365 (2017).
- Zhang, B. et al. Homogeneously dispersed multimetal oxygen-evolving catalysts. *Science* **352**, 333–337 (2016).
- Yang, H. et al. Intramolecular hydroxyl nucleophilic attack pathway by a polymeric water oxidation catalyst with single cobalt sites. *Nat. Catal.* **5**, 414–429 (2022).
- Man, I. C. et al. Universality in oxygen evolution electrocatalysis on oxide surfaces. *ChemCatChem* **3**, 1159–1165 (2011).
- Montoya, J. H. et al. Materials for solar fuels and chemicals. *Nat. Mater.* **16**, 70–81 (2016).
- Huang, Z.-F. et al. Strategies to break the scaling relation toward enhanced oxygen electrocatalysis. *Matter* **1**, 1494–1518 (2019).
- Roger, I., Shipman, M. A. & Symes, M. D. Earth-abundant catalysts for electrochemical and photoelectrochemical water splitting. *Nat. Rev. Chem.* **1**, 0003 (2017).
- Matheu, R. et al. The development of molecular water oxidation catalysts. *Nat. Rev. Chem.* **3**, 331–341 (2019).
- Huang, Z.-F. et al. Tuning of lattice oxygen reactivity and scaling relation to construct better oxygen evolution electrocatalyst. *Nat. Commun.* **12**, 3992–4000 (2021).
- Fei, H. et al. General synthesis and definitive structural identification of MN_4C_4 single-atom catalysts with tunable electrocatalytic activities. *Nat. Catal.* **1**, 63–72 (2018).
- Bai, L., Hsu, C.-S., Alexander, D. T. L., Chen, H. M. & Hu, X. Double-atom catalysts as a molecular platform for heterogeneous oxygen evolution electrocatalysis. *Nat. Energy* **6**, 1054–1066 (2021).
- Li, S. et al. Oxygen-evolving catalytic atoms on metal carbides. *Nat. Mater.* **20**, 1240–1247 (2021).
- Doyle, A. D., Montoya, J. H. & Vojvodic, A. Improving oxygen electrochemistry through nanoscopic confinement. *ChemCatChem* **7**, 738–742 (2015).
- Qiu, T., Tu, B. T., Saldana-Greco, D. & Rappe, A. M. Ab initio simulation explains the enhancement of catalytic oxygen evolution on CaMnO_3 . *ACS Catal.* **8**, 2218–2224 (2018).
- Halck, N. B., Petrykin, V., Krtíl, P. & Rossmel, J. Beyond the volcano limitations in electrocatalysis–oxygen evolution reaction. *Phys. Chem. Chem. Phys.* **16**, 13682–13688 (2014).
- She, S. et al. Realizing ultrafast oxygen evolution by introducing proton acceptor into Perovskites. *Adv. Energy Mater.* **9**, 1900429 (2019).
- Zhao, G., Li, P., Cheng, N., Dou, S. X. & Sun, W. An Ir/Ni(OH)_2 heterostructured electrocatalyst for the oxygen evolution reaction: breaking the scaling relation, stabilizing iridium(V), and beyond. *Adv. Mater.* **32**, 2000872 (2020).
- Gao, Z.-W. et al. Engineering NiO/NiFe LDH intersection to bypass scaling relationship for oxygen evolution reaction via dynamic tridimensional adsorption of intermediates. *Adv. Mater.* **31**, 1804769 (2019).
- Ma, P. et al. Modulating hydrogen bonding in single-atom catalysts to break scaling relation for oxygen evolution. *Chem. Catal.* **2**, 2764 (2022).
- Fabbri, E. et al. Dynamic surface self-reconstruction is the key of highly active perovskite nano-electrocatalysts for water splitting. *Nat. Mater.* **16**, 925–931 (2017).
- Cao, L. et al. Identification of single-atom active sites in carbon-based cobalt catalysts during electrocatalytic hydrogen evolution. *Nat. Catal.* **2**, 134–141 (2019).
- Cao, L. et al. Dynamic oxygen adsorption on single-atomic ruthenium catalyst with high performance for acidic oxygen evolution reaction. *Nat. Commun.* **10**, 4849 (2019).
- Yang, J. et al. Potential-driven restructuring of Cu single atoms to nanoparticles for boosting the electrochemical reduction of nitrate to ammonia. *J. Am. Chem. Soc.* **144**, 12062–12071 (2022).
- Yang, J. et al. Dynamic behavior of single-atom catalysts in electrocatalysis: identification of Cu-N_3 as an active site for the oxygen reduction reaction. *J. Am. Chem. Soc.* **143**, 14530–14539 (2021).
- Hai, X. et al. Geminal-atom catalysis for cross-coupling. *Nature* **622**, 754–760 (2023).
- Chen, Z., Liu, Z. & Xu, X. Dynamic evolution of the active center driven by hemilabile coordination in Cu/CeO_2 single-atom catalyst. *Nat. Commun.* **14**, 2512 (2023).
- Pérez-Ramírez, J. & López, N. Strategies to break linear scaling relationships. *Nat. Catal.* **2**, 971–976 (2019).
- Trotochaud, L., Young, S. L., Ranney, J. K. & Boettcher, S. W. Nickel-iron oxyhydroxide oxygen-evolution electrocatalysts: the role of intentional and incidental iron incorporation. *J. Am. Chem. Soc.* **136**, 6744–6753 (2014).
- Hu, C. et al. Spontaneous reduction and assembly of graphene oxide into three-dimensional graphene network on arbitrary conductive substrates. *Sci. Rep.* **3**, 2065 (2013).
- Yang, H. B. et al. Atomically dispersed Ni(I) as the active site for electrochemical CO_2 reduction. *Nat. Energy* **3**, 140–147 (2018).
- Bai, L., Hsu, C.-S., Alexander, D. T. L., Chen, H. M. & Hu, X. A cobalt-iron double-atom catalyst for the oxygen evolution reaction. *J. Am. Chem. Soc.* **141**, 14190–14199 (2019).
- Chen, J. Y. et al. Operando analysis of NiFe and Fe oxyhydroxide electrocatalysts for water oxidation: detection of Fe^{4+} by Mossbauer spectroscopy. *J. Am. Chem. Soc.* **137**, 15090–15093 (2015).
- Zhang, Z. et al. In-situ generated high-valent iron single-atom catalyst for efficient oxygen evolution. *Nano Lett.* **21**, 4795–4801 (2021).
- Gorlin, Y. et al. In situ X-ray absorption spectroscopy investigation of a bifunctional manganese oxide catalyst with high activity for electrochemical water oxidation and oxygen reduction. *J. Am. Chem. Soc.* **135**, 8525–8534 (2013).
- Wang, J. et al. In situ X-ray spectroscopies beyond conventional X-ray absorption spectroscopy on deciphering dynamic configuration of electrocatalysts. *Nat. Commun.* **14**, 6576 (2023).
- Yamamoto, T. Assignment of pre-edge peaks in K-edge X-ray absorption spectra of 3d transition metal compounds: electric dipole or quadrupole? *Xray Spectrom.* **37**, 572–584 (2008).
- Colpas, G. J. et al. X-ray spectroscopic studies of nickel complexes, with application to the structure of nickel sites in hydrogenases. *Inorg. Chem.* **30**, 920–928 (1991).
- Rossi, G., d’Acapito, F., Amidani, L., Boscherini, F. & Pedio, M. Local environment of metal ions in phthalocyanines: K-edge X-ray absorption spectra. *Phys. Chem. Chem. Phys.* **18**, 23686–23694 (2016).
- Pan, Y. et al. Regulating the coordination structure of single-atom $\text{Fe-N}_x\text{C}_y$ catalytic sites for benzene oxidation. *Nat. Commun.* **10**, 4290 (2019).

44. Wang, J. et al. In situ formation of molecular Ni-Fe active sites on heteroatom-doped graphene as a heterogeneous electrocatalyst toward oxygen evolution. *Sci. Adv.* **4**, eaap7970 (2018).
45. Sun, L. et al. A planar, conjugated N₄-macrocyclic cobalt complex for heterogeneous electrocatalytic CO₂ reduction with high activity. *Angew. Chem. Int. Ed.* **59**, 17104–17109 (2020).
46. Chung, D. Y. et al. Dynamic stability of active sites in hydr(oxy) oxides for the oxygen evolution reaction. *Nat. Energy* **5**, 222–230 (2020).
47. Giordano, L. et al. pH dependence of OER activity of oxides: current and future perspectives. *Catal. Today* **262**, 2–10 (2016).
48. Fang, Y.-H. & Liu, Z.-P. Tafel kinetics of electrocatalytic reactions: from experiment to first-principles. *ACS Catal.* **4**, 4364–4376 (2014).
49. Hao, Y. et al. Recognition of surface oxygen intermediates on NiFe oxyhydroxide oxygen-evolving catalysts by homogeneous oxidation reactivity. *J. Am. Chem. Soc.* **143**, 1493–1502 (2021).
50. Bai, L., Lee, S. & Hu, X. Spectroscopic and electrokinetic evidence for a bifunctional mechanism of the oxygen evolution reaction. *Angew. Chem. Int. Ed.* **60**, 3095–3103 (2021).
51. Tao, H. B. et al. A general method to probe oxygen evolution intermediates at operating conditions. *Joule* **3**, 1498–1509 (2019).
52. Huang, Z.-F. et al. Chemical and structural origin of lattice oxygen oxidation in Co–Zn oxyhydroxide oxygen evolution electrocatalysts. *Nat. Energy* **4**, 329–338 (2019).
53. Hummers, W. S. & Offeman, R. E. Preparation of graphitic oxide. *J. Am. Chem. Soc.* **80**, 1339–1339 (1958).
54. Du, Y. et al. XAFCA: a new XAFS beamline for catalysis research. *J. Synchrotron Radiat.* **22**, 839–843 (2015).
55. Ravel, B. & Newville, M. ATHENA, ARTEMIS, HEPHAESTUS: data analysis for X-ray absorption spectroscopy using IFEFFIT. *J. Synchrotron Radiat.* **12**, 537–541 (2005).
56. McCrory, C. C. L., Jung, S., Peters, J. C. & Jaramillo, T. F. Benchmarking heterogeneous electrocatalysts for the oxygen evolution reaction. *J. Am. Chem. Soc.* **135**, 16977–16987 (2013).
57. Bard, A. J., Parsons, R. & Jordan, J. *Standard Potentials in Aqueous Solution* (Routledge, 1985).
58. Li, W. et al. A bio-inspired coordination polymer as outstanding water oxidation catalyst via second coordination sphere engineering. *Nat. Commun.* **10**, 5074 (2019).
59. Kohn, W. & Sham, L. J. Self-consistent equations including exchange and correlation effects. *Phys. Rev.* **140**, 1133–1138 (1965).
60. Kresse, G. & Furthmüller, J. Efficient iterative schemes for ab initio total-energy calculations using a plane-wave basis set. *Phys. Rev. B* **54**, 11169–11186 (1996).
61. Kresse, G. & Furthmüller, J. Efficiency of ab-initio total energy calculations for metals and semiconductors using a plane-wave basis set. *Comp. Mater. Sci.* **6**, 15–50 (1996).
62. Perdew, J. P., Burke, K. & Ernzerhof, M. Generalized gradient approximation made simple. *Phys. Rev. Lett.* **77**, 3865–3868 (1996).
63. Frisch, M. J. et al. *Gaussian 16, Revision C.01* (Gaussian, 2016).
64. Nørskov, J. K. et al. Origin of the overpotential for oxygen reduction at a fuel-cell cathode. *J. Phys. Chem. B* **108**, 17886–17892 (2004).
65. VandeVondele, J. et al. Quickstep: fast and accurate density functional calculations using a mixed Gaussian and plane waves approach. *Comput. Phys. Commun.* **167**, 103–128 (2005).
66. Nosé, S. A unified formulation of the constant temperature molecular dynamics methods. *J. Chem. Phys.* **81**, 511–519 (1984).
67. Hoover, W. G. Canonical dynamics: equilibrium phase-space distributions. *Phys. Rev. A* **31**, 1695–1697 (1985).
68. Sprik, M. & Ciccotti, G. Free energy from constrained molecular dynamics. *J. Chem. Phys.* **109**, 7737–7744 (1998).
69. Zhang, Z. et al. Breaking linear scaling relationships in oxygen evolution via dynamic structural regulation of active sites. *Figshare*. <https://doi.org/10.6084/m9.figshare.27086794> (2024).

Acknowledgements

This work was financially supported by a grant (No. CHI-P2022-04) from Centre for Hydrogen Innovations at National University of Singapore. B.L. acknowledges support from the City University of Hong Kong startup fund (No. 9020003), ITF–RTH - Global STEM Professorship (No. 9446006), and JC STEM Lab of Advanced CO₂ Upcycling (No. 9228005). Y.-G.W. acknowledges financial support from the National Natural Science Foundation of China (No. 22022504), NSFC Center for Single-Atom Catalysis (No. 22388102), the Guangdong “Pearl River” Talent Plan (No. 2019QN01L353), and the Science, Technology and Innovation Commission of Shenzhen Municipality (No. JCYJ20210324103608023). X.Z. acknowledges the National Key R&D Program of China (No. 2024YFE0109200). We acknowledge the XAS measurements at the XAFCA and SUV beamlines of SSLS and the computing resources from National Supercomputing Centre, Singapore for XANES simulations.

Author contributions

P.C., B.L., and Z.Z. conceived and designed the project. Z.Z. performed the catalyst synthesis, most of the structural characterizations and electrochemical tests. H.Z. and Y.-G.W. carried out the theoretical calculations. S.X. performed the operando XAFS measurements and XANES simulations. X.Z. performed the aberration-corrected HAADF-STEM. X.C. and X.Y. performed the soft XAS measurements. H.B.Y. and Z.C. assisted with data analysis and paper revision. P.C., B.L., Z.Z., H.Z., S.X., and Y.-G.W. co-wrote the paper. All the authors reviewed and contributed to this paper.

Competing interests

The authors declare no competing interests.

Additional information

Supplementary information The online version contains supplementary material available at <https://doi.org/10.1038/s41467-024-55150-9>.

Correspondence and requests for materials should be addressed to Yang-Gang Wang, Bin Liu or Peng Chen.

Peer review information *Nature Communications* thanks Fang Song and the other anonymous reviewer(s) for their contribution to the peer review of this work. A peer review file is available.

Reprints and permissions information is available at <http://www.nature.com/reprints>

Publisher's note Springer Nature remains neutral with regard to jurisdictional claims in published maps and institutional affiliations.

Open Access This article is licensed under a Creative Commons Attribution-NonCommercial-NoDerivatives 4.0 International License, which permits any non-commercial use, sharing, distribution and reproduction in any medium or format, as long as you give appropriate credit to the original author(s) and the source, provide a link to the Creative Commons licence, and indicate if you modified the licensed material. You do not have permission under this licence to share adapted material derived from this article or parts of it. The images or other third party material in this article are included in the article's Creative Commons licence, unless indicated otherwise in a credit line to the material. If material is not included in the article's Creative Commons licence and your intended use is not permitted by statutory regulation or exceeds the permitted use, you will need to obtain permission directly from the copyright holder. To view a copy of this licence, visit <http://creativecommons.org/licenses/by-nc-nd/4.0/>.

© The Author(s) 2025